INORGANIC CHEMISTRY FRONTIERS

RESEARCH ARTICLE

View Article Online
View Journal

Cite this: DOI: 10.1039/d5qi00966a

High loading of iridium single atoms in $NiCo_2O_4$ for enhanced acidic oxygen evolution reaction†

Bilal Zaman,‡ Qiwen Su,‡ Dongxu Jiao, Ming Gong, Mingming Wang, Muhammad Faizan and Xiaoqiang Cui *

Received 16th April 2025,
Accepted 23rd June 2025

DOI: 10.1039/d5qi00966a

rsc.li/frontiers-inorganic

The development of high loading single-atom electrocatalysts presents significant potential for enhancing the performance of the acidic oxygen evolution reaction (OER). Herein, a high loading (7.98 wt%) iridium single atom doped $NiCo_2O_4$ (Ir_H-$NiCo_2O_4$) catalyst was prepared using an ion-exchange pyrolysis method. The optimized Ir_H-$NiCo_2O_4$ demonstrated an enhanced OER performance, achieving an overpotential of 240 mV at a current density of 10 mA cm^{-2}, along with exceptional stability for over 282 hours in a 0.5 M H_2SO_4 solution. Additionally, it demonstrated an overall mass activity of 377.05 mA mg_{Ir}^{-1} at a 300 mV OER overpotential, surpassing the performance of commercial IrO_2. Density functional theory calculations revealed that the high-density of Ir-single atom doping enhances the adsorption energy of oxygen-containing intermediates, thereby promoting the OER process. This study offers a viable strategy for fabricating high-loading single-atom catalysts, offering insights that can be generalized to other systems and paving the way for advancing their industrial-scale applications.

1. Introduction

Hydrogen, a clean and sustainable energy carrier, can be efficiently produced through electrochemical water splitting, driven by renewable energy sources such as solar and wind power.[1–7] Among the available technologies, proton exchange membrane (PEM) water electrolysis is recognized as a highly promising method due to its advantages, including high current density, excellent energy efficiency, and rapid system responsiveness.[8–13] To date, iridium (Ir)-based catalysts are widely regarded as the most viable materials for facilitating the oxygen evolution reaction (OER) in PEM water electrolyzers, primarily because of their exceptional stability under acidic conditions.[14–16] However, the high cost of Ir (US$3950 per troy ounce) and its limited natural abundance[17] pose significant barriers to scaling-up Ir-containing catalysts for industrial applications.[14,18,19] Therefore, developing low cost Ir-based electrocatalysts with enhanced activity and high durability is urgent, but remains a significant challenge.

Recently, single-atom catalysts (SACs) have gained significant interest for electrochemical reactions, owing to their exceptional advantages, such as unique active sites, high product selectivity, enhanced atomic efficiency, a variety of support materials, and reduced consumption of noble metals.[20–23] The most reported SACs are characterized by low metal loadings, typically less than 1 wt%, to ensure atomic dispersion.[24–26] For instance, Li *et al.* achieved an overpotential of 246 mV (at j = 10 mAcm^{-2}) and enhanced stability for 160 h by incorporating a 0.2 wt% Ir single-atom into Co_3O_4.[27] Similarly, Luo *et al.* utilized a double protecting strategy to fabricate an atomically dispersed Ir single-atom catalyst with a loading of 0.4 wt% (Ir-SA@Fe@NCNT). Ir-SA@Fe@NCNT exhibited enhanced OER performance with an overpotential of 250 mV at a standard current density of 10 mA cm^{-2} and high catalytic stability for continuous 12 hours under acidic conditions.[28] However, the inherently low metal loadings in SACS significantly constrain their overall catalytic performance and limit their potential applications, particularly for industrial scale applications.[29] Thus, there is an urgent need to design high-loading Ir single atom catalysts that combine superior activity and long-term stability to meet the increasing energy demands.

Spinel structure transition metal-oxides have emerged as strong candidates for electrocatalysis, owing to their excellent electrocatalytic activity.[30] In particular, spinel oxides such as $NiCo_2O_4$ have gained significant attention because of their high natural abundance, large electrical conductivity, and improved OER activity.[31–33] For example, Wang *et al.* synthesized Ru-doped $NiCo_2O_4$ on nickel foam, reporting a 249 mV overpotential at a current density of 10 mA cm^{-2} with 30 hours of catalytic stability in alkaline solution.[34] Similarly,

State Key Laboratory of Automotive Simulation and Control, School of Materials Science and Engineering, and Key Laboratory of Automobile Materials of MOE, Jilin University, Changchun, 130012, China. E-mail: xqcui@jlu.edu.cn

†Electronic supplementary information (ESI) available. See DOI: https://doi.org/10.1039/d5qi00966a

‡These authors contributed equally to this work.

Tao *et al.* doped molybdenum (Mo) into $NiCo_2O_4$ (Mo-$NiCo_2O_4$) and enhanced the overall OER performance using the facile hydrothermal method. With a ~1.95 wt% Mo, they achieved a low overpotential of magnitude 265 mV measured at a current density of 10 mA cm^{-2} with high stability for 100 hours in 0.1 M KOH.[35] However, $NiCo_2O_4$ only exhibits electrocatalytic activity for the OER in alkaline electrolytes. Developing spinel-type $NiCo_2O_4$ catalysts with improved OER activity and high stability under acidic conditions remains a key challenge. Therefore, it would be a significant advancement if high loading Ir single atoms could be doped into $NiCo_2O_4$ for the OER in acidic media.

In this study, we report the successful synthesis of a high loading (7.98 wt%) Ir single atom doped (Ir_H-$NiCo_2O_4$) catalyst through an ion exchange-pyrolysis approach. The resulting catalyst exhibits remarkable OER activity (*i.e.*, achieving an overpotential of 240 mV at 10 mA cm^{-2}) and demonstrates high catalytic stability for 282 hours in acidic solutions. Density functional theory (DFT) calculations show that the high-density of Ir-single atom doping significantly enhances the adsorption energy of oxygen-containing intermediates, thereby promoting the OER process. This study provides a strategic framework for the rational design of highly stable, high loading single atom catalysts (SACs) towards OER applications under acidic conditions, paving the way for future developments in the field.

2. Experimental section

2.1. Materials

Carbon paper was supplied by "Tianjin IncoleUnion Tech. Co., Ltd". A variety of chemicals, including 2-methylimidazole ($C_4H_6N_2$, ≥98%), ethanol (CH_3CH_2OH, ≥97.7%), nickel(II) nitrate-hexahydrate [($Ni(NO_3)_2{\cdot}6H_2O$, ≥98%)], iridium chloride-hydrate ($IrCl_3{\cdot}xH_2O$, ≥99.98%), methanol (CH_3OH, ≥99.5%), Nafion (5%), hexadecyltrimethylammonium bromide (CTAB, ≥99%), cobalt(II) nitrate-hexahydrate [($Co(NO_3)_2{\cdot}6H_2O$, ≥98.5%)], sulphuric acid (H_2SO_4, ≥98%), and commercial iridium oxide (IrO_2, ≥99.9%), were bought from Macklin. Additionally, all of these compounds were utilized as supplied, without further purification. Furthermore, high-purity deionized H_2O with a resistivity of '18.2 MΩ cm^{-1}' was employed as the solvent in all tests, guaranteeing the integrity and dependability of the results.

2.2. Synthesis of Ir_H-$NiCo_2O_4$

The synthesis of ZIF-67 was carried out following a well-established surfactant-mediated method.[36] Firstly, cobalt(II) nitrate hexahydrate ($Co(NO_3)_2{\cdot}6H_2O$) (580 mg) was dissolved in 20 mL of deionized H_2O containing 30 mg of CTAB. Secondly, this solution was then added to 140 mL of an aqueous solution containing 9.08 g of 2-methylimidazole, and the mixture was stirred at room temperature for about 60 minutes. The resulting purple precipitates underwent centrifugation followed by washing with ethanol five times. Finally, the ZIF-67 nanocrystals were produced by drying the precipitates in a vacuum oven overnight at 60 °C.

The Ir_H-$NiCo_2O_4$ catalyst was prepared through an ion exchange technique which was followed by pyrolysis. Initially, ZIF-67 nanocrystals (50 mg) and nickel(II) nitrate-hexahydrate ($Ni(NO_3)_2{\cdot}6H_2O$) (0.5 mmol) were dissolved in a 25 mL methanol solution. The solution was continuously stirred for about 20 minutes to carry out the ion exchange reaction. Subsequently, 4 mL of the iridium chloride ($IrCl_3{\cdot}xH_2O$) solution having a concentration of 2.5 mg mL^{-1} was added dropwise to the ZIF-67 solution under stirring conditions. After 15 minutes, the reaction was quenched by centrifugation, and the resulting precipitates were collected and dried in a vacuum oven (60 °C) for a whole night. Finally, the dried precipitates were calcined in air for 2 hours at 400 °C to obtain the Ir_H-$NiCo_2O_4$ catalyst.

2.3. Synthesis of Ir_L-$NiCo_2O_4$

The electrocatalyst with a low Ir loading (Ir_L-$NiCo_2O_4$) was synthesized by employing a procedure similar to that used for Ir_H-$NiCo_2O_4$, but with the addition of only 2 mL of 2.5 mg mL^{-1} iridium chloride ($IrCl_3{\cdot}xH_2O$) solution.

2.4. Synthesis of $NiCo_2O_4$

A pure $NiCo_2O_4$ electrocatalyst was also synthesized by employing the same protocols as for the catalyst 'Ir_H-$NiCo_2O_4$', but in the absence of $IrCl_3{\cdot}xH_2O$.

2.5. Characterization

The synthesized catalysts were comprehensively characterized by employing a variety of methods to determine their structural, compositional, and morphological properties; namely, insight into the sample's crystal structure was obtained through X-ray diffraction (XRD) using a Bragg–Brentano diffractometer (D8-Tools, Germany). The morphological characteristics were examined using scanning electron microscopy (SEM, SU8010, Hitachi) and transmission electron microscopy (TEM, JEM-2100F, JEOL, Japan). High-angle annular dark field scanning TEM (HAADF-STEM) and energy-dispersive X-ray spectroscopy (EDX) mapping of the as-prepared catalysts were performed using aberration-corrected scanning transmission electron microscopy (JEOL ARM200CF, Japan). The surface chemical composition was investigated by means of X-ray photoelectron spectroscopy (XPS) with a Thermo ESCALAB-250 instrument (Thermo Fisher Scientific, USA). The elemental concentrations and compositions of the synthesized samples were determined *via* inductively coupled plasma-mass spectrometry (ICP-MS) with an ELAN 9000/DRC system. Furthermore, the magnetic properties of the synthesized samples were studied by recording electron paramagnetic resonance (EPR) spectra at room temperature using a Bruker-A300 EPR-spectrometer (Shanghai, China).

2.6. Electrochemical characterization

The electrochemical properties of all the prepared samples were evaluated in a 0.5 M H_2SO_4 electrolyte using a three-electrode setup connected to an electrochemical workstation (CHI

760E). The catalyst was loaded onto carbon paper with an 'Ir' loading of 0.25 mg cm^{-2}. The working electrode consisted of a carbon paper electrode coated with the fabricated catalyst, while Hg/Hg_2Cl_2 and a carbon rod were used as the reference and counter electrodes, respectively. All the recorded potentials were converted to reversible hydrogen-electrode scales using the following relation: [E(RHE) = 0.242 + 0.059 pH + $E(Hg/Hg_2Cl_2)$]. The polarization curves for the OER were calculated through the linear sweep voltammetry technique at a scan rate of 5 mVs^{-1} and were corrected using the automatic iR compensation function of the workstation. Additionally, the electrochemical double-layer capacitance of the prepared catalysts was determined using cyclic voltammetry in the non-faradaic region at scan rates varying from 10 to 200 mV s^{-1}.

To further investigate the electrochemical properties of the produced samples, electrochemical impedance spectroscopy (EIS) measurements were performed over the frequency range of 0.01–100 kHz with a voltage amplitude of 5 mV. We also assessed the electrocatalytic activity of commercial IrO_2 with an Ir loading of 0.8 mg cm^{-2} on carbon paper for comparison purposes.

2.7. Theoretical calculations

We performed spin–polarized density functional theory (DFT) calculations by employing the Vienna *Ab initio* Simulation Package (VASP)[37,38] with the projector augmented wave (PAW) method.[39,40] The Perdew–Burke–Ernzerhof (PBE)[41] functional was used within a generalized gradient approximation (GGA). Grimme's zero damping DFT-D3 method was used to account for the van der Waals interactions, with a cutoff energy of 500 eV.[42] The lattice plane of (220) was constructed from the $NiCo_2O_4$ material and fully optimized within a $\sqrt{2} \times \sqrt{2} \times 1$ supercell during structural relaxation. A vacuum space of 20 Å was adopted in the z direction to minimize interactions between periodic images. The reciprocal space was sampled using a 3 × 3 × 1 k-point mesh, and the structures were fully relaxed until the maximum residual force was less than 0.05 eV $Å^{-1}$. The energy convergence threshold was established at 10^{-5} eV.

The Gibbs free energy change (ΔG) for each elementary step of the OER was computed using the computational hydrogen electrode (CHE) model.[43,44] According to this model, the ΔG value is expressed as follows: $\Delta G = \Delta E + \Delta ZPE - T\Delta S$, where ΔE represents the reaction energy of the reactant and product species adsorbed on the catalyst, directly obtained from DFT computations, and ΔZPE and ΔS represent the changes between the adsorbed species and gas-phase molecules in zero-point energies and entropy at 298.15 K, derived from vibrational frequencies. The OER overpotential (η) was calculated as η = max $(-\Delta G_1, -\Delta G_2, -\Delta G_3, -\Delta G_4)/e - 1.23$ V. According to this definition, a smaller η value indicates a higher OER catalytic activity.

3. Results and discussion

3.1. Structural characterization

Ir_H-$NiCo_2O_4$ and Ir_L-$NiCo_2O_4$ catalysts were obtained using an ion exchange pyrolysis protocol mediated by metal–organic frameworks as illustrated in Fig. S1.† For comparison, pure $NiCo_2O_4$ was also prepared using the same protocols but in the absence of the Ir precursor (Fig. S2 and Table S1†). Scanning electron microscopy was employed to characterize the morphology of the ZIF-67 precursor, pure $NiCo_2O_4$, Ir_L-$NiCo_2O_4$, and Ir_H-$NiCo_2O_4$ catalysts. The SEM image of the ZIF-67 precursor shows nanocube-like morphology (Fig. S3†), while $NiCo_2O_4$ exhibits a nanocage-like morphology (Fig. 1a). When Ir is introduced into $NiCo_2O_4$, the resultant Ir_L-$NiCo_2O_4$ and Ir_H-$NiCo_2O_4$ catalysts exhibit similar morphological features to pure $NiCo_2O_4$, declaring that introducing 'Ir' does not ruin the nanocage-structure of $NiCo_2O_4$ (Fig. 1b and c). The morphology of pure $NiCo_2O_4$, Ir_L-$NiCo_2O_4$ and Ir_H-$NiCo_2O_4$ was further confirmed by the transmission electron microscopy (TEM) images (Fig. 1d–f). The TEM images of pure $NiCo_2O_4$, Ir_L-$NiCo_2O_4$ and Ir_H-$NiCo_2O_4$ are structured as nanocages, where the pure $NiCo_2O_4$ nanocages are composed of nanoparticles. Meanwhile, the selected area electron diffraction (SAED) pattern of Ir_H-$NiCo_2O_4$ further confirms the (400), (311) and (220) lattice planes of $NiCo_2O_4$ (inset of Fig. 1f). To determine the distribution of Ir species, the high angle annular dark field-scanning transmission electron microscopy (HAADF-STEM) images were collected for Ir_H-$NiCo_2O_4$ (Fig. 1g, Fig. S4a and b†). The HAADF-STEM images revealed bright spots marked by red circles which are assigned to Ir single atoms and Ir_H-$NiCo_2O_4$ exhibits lattice spacings of 0.29 nm and 0.25 nm, which can be ascribed to the (220) and (311) planes of $NiCo_2O_4$, respectively. The crystal structures of pure $NiCo_2O_4$, Ir_L-$NiCo_2O_4$, and Ir_H-$NiCo_2O_4$ catalysts were characterized using an X-ray diffractometer. As shown in Fig. 1h, the diffraction peaks of pure $NiCo_2O_4$ can match well with those of cubic $NiCo_2O_4$ (JCPDS No. 20-0781, space group F^*3). The Ir_L-$NiCo_2O_4$ and Ir_H-$NiCo_2O_4$ catalysts exhibit similar diffraction peaks to pure $NiCo_2O_4$, but without the related Ir oxide phase being detected, implying that the Ir single atom was doped successfully into $NiCo_2O_4$. Elemental mapping images also show homogeneous dispersion of Ir, Ni, Co, and O atoms throughout the entire Ir_H-$NiCo_2O_4$ sample (Fig. 1i). Moreover, the inductively coupled plasma (ICP) analysis (Table S2†) reveals that the Ir content in Ir_H-$NiCo_2O_4$ is 7.98%. The ICP analysis of Ir_H-$NiCo_2O_4$ and pure $NiCo_2O_4$ indicates that Ir replaces Ni and Co. In general, the combined valence states of both nickel and cobalt may typically occupy tetrahedral and octahedral sites in pure $NiCo_2O_4$, demonstrating enhanced electrical conductivity and electrocatalytic activity.[45] In spinel formations like $NiCo_2O_4$, Co^{2+} and Co^{3+} occupy tetrahedral sites, whereas Co^{3+}, Ni^{2+}, and Ni^{3+} reside in octahedral sites.[45] Furthermore, Ir^{3+} and Ir^{4+} ions are likely to occupy certain octahedral sites due to the strong affinity of the ligands for these positions.[46,47] Additionally, it has been documented that the octahedral positions in the spinel structures of $LiIr_2O_4$ and $CuIr_2S_4$ contain Ir atoms.[48,49] Therefore, it is expected that Ni^{2+}, Ni^{3+}, and Co^{3+} situated at the octahedral sites in $NiCo_2O_4$ are replaced by Ir, resulting in the formation of the Ir_H-$NiCo_2O_4$ structure.

X-ray photoelectron spectroscopy (XPS) was used to analyze the electronic structures and surface chemical states of the

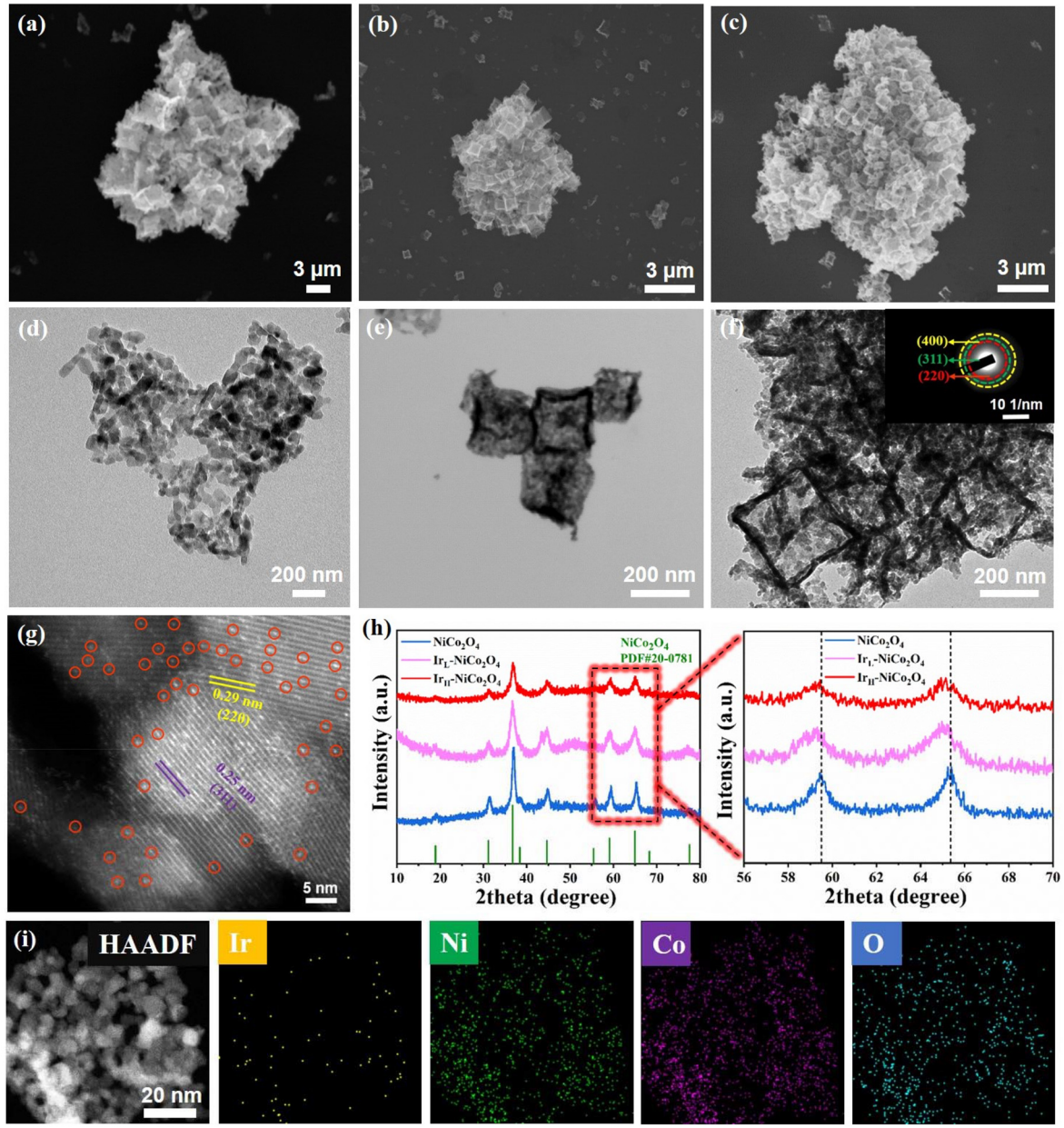

Fig. 1 (a–c) SEM images of pure $NiCo_2O_4$, Ir_L-$NiCo_2O_4$ and Ir_H-$NiCo_2O_4$. (d–f) TEM images of pure $NiCo_2O_4$, Ir_L-$NiCo_2O_4$ and Ir_H-$NiCo_2O_4$. The inset in (f) depicts the SAED image of Ir_H-$NiCo_2O_4$. (g) HAADF-STEM image of Ir_H-$NiCo_2O_4$, in which the bright spots marked by red circles are ascribed to Ir single atoms. (h) XRD patterns of pure $NiCo_2O_4$ and Ir-$NiCo_2O_4$. (i) The corresponding elemental mapping images of Ir_H-$NiCo_2O_4$.

synthesized materials. The XPS survey spectra shown in Fig. S5† offer a comprehensive analysis of the elemental composition of pure $NiCo_2O_4$, Ir_L-$NiCo_2O_4$, and Ir_H-$NiCo_2O_4$ catalysts. To establish precise peak assignments, the spectra were calibrated with the C 1s at 284.8 eV. Fig. 2a shows a comparison of the Ir 4f XPS spectra of Ir_H-$NiCo_2O_4$, Ir_L-$NiCo_2O_4$, and commercial IrO_2. The peaks at 61.3 and 64.1 eV were assigned to Ir^{4+} $4f_{7/2}$ and Ir^{4+} $4f_{5/2}$, respectively.[50,51] Additionally, the peaks at 62.3 and 65.5 eV were allocated to Ir^{3+} $4f_{7/2}$ and Ir^{3+} $4f_{5/2}$, respectively.[50,51] Notably, the XPS spectra of Ir 4f shift to lower binding energies compared to commercial IrO_2, suggesting the lower valence states of Ir in Ir_H-$NiCo_2O_4$.[52] Generally, the low valence state of Ir^{n+} ($n < 4$) often inhibits Ir oxides from undergoing further oxidation to higher valence states (*e.g.*, unstable Ir^{6+} species), hence preventing dissolution during the acidic OER process.[53–55] Additionally, the peak located at 60.7 eV is produced by Co 3p. The Ni 2p spectrum in Fig. 2b shows two distinct peaks at 872.42 eV and 854.90 eV, which correspond to Ni $2p_{1/2}$ and Ni $2p_{3/2}$, respectively. This signature confirms the presence of Ni^{2+} in pure $NiCo_2O_4$, Ir_L-$NiCo_2O_4$ and Ir_H-$NiCo_2O_4$ samples. Notably, the peaks identified at 873.44 eV and 855.77 eV corresponded to Ni $2p_{1/2}$ and Ni $2p_{3/2}$ of Ni^{3+}, respectively.[56] Moreover, satellite peaks for Ni^{2+} and Ni^{3+} were also seen at 862.22 eV and 880.94 eV,

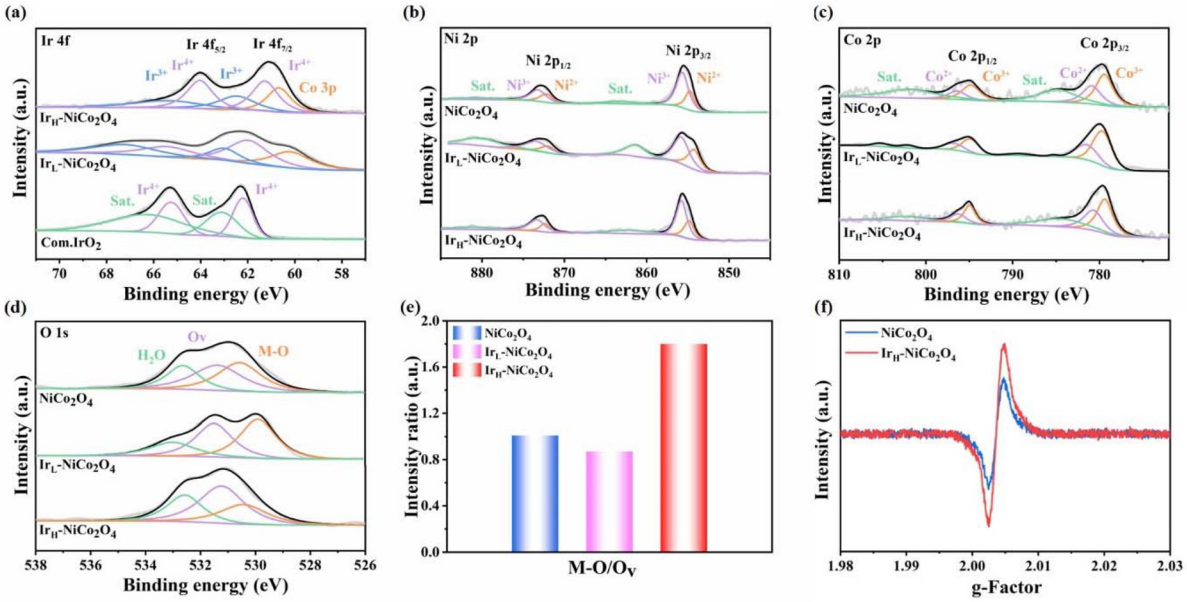

Fig. 2 High-resolution XPS spectra. (a) Ir 4f spectra of Ir_H-$NiCo_2O_4$, Ir_L-$NiCo_2O_4$ and Com·IrO_2. (b) Ni 2p, (c) Co 2p and (d) O 1s XPS spectra of pure $NiCo_2O_4$, Ir_L-$NiCo_2O_4$ and Ir_H-$NiCo_2O_4$. (e) The ratio of M–O/O_v for pure $NiCo_2O_4$, Ir_L-$NiCo_2O_4$ and Ir_H-$NiCo_2O_4$. (f) EPR spectra of $NiCo_2O_4$ and Ir_H-$NiCo_2O_4$.

respectively.[57] Remarkably, the peak of Ni $2p_{3/2}$ in Ir_H-$NiCo_2O_4$ exhibits a slight shift towards positive binding energy relative to pure $NiCo_2O_4$.

The high-resolution Co 2p spectra (Fig. 2c) reveal the identification of two peaks corresponding to Co $2p_{1/2}$ and Co $2p_{3/2}$ in pure $NiCo_2O_4$, Ir_L-$NiCo_2O_4$ and Ir_H-$NiCo_2O_4$. For Ir_H-$NiCo_2O_4$, the peaks at 779.3 eV and 780.7 eV were attributed to Co^{3+} $2p_{3/2}$ and Co^{2+} $2p_{3/2}$, respectively, whereas the remaining peaks represent Co 2p satellite features. Additionally, the peaks observed at 794.9 and 796.3 eV were ascribed to Co^{3+} $2p_{1/2}$ and Co^{2+} $2p_{1/2}$, respectively. Compared to pure $NiCo_2O_4$, the specific locations of Co 2p in Ir_H-$NiCo_2O_4$ were displaced towards lower binding energy.[34,58] The O 1s XPS spectra of the pure $NiCo_2O_4$, Ir_L-$NiCo_2O_4$ and Ir_H-$NiCo_2O_4$ samples were evaluated (Fig. 2d) to assess the influence of elemental oxygen. The distinct peaks seen at 530.41, 531.24, and 532.57 eV are assigned to the metal–oxygen (M–O) bond, oxygen vacancies (O_v), and water-adsorbed oxygen (H_2O), respectively.[59] Moreover, the ratio of O_v/M–O peak area can be employed to calculate the relative concentration of surface oxygen vacancies, where a higher ratio suggests a higher quantity of oxygen vacancies (Fig. 2e).[60–63] The ratio of O_v/M–O for Ir_H-$NiCo_2O_4$ is 1.80, which is significantly higher than that of Ir_L-$NiCo_2O_4$ (0.87) and $NiCo_2O_4$ (1.01), indicating an increased concentration of oxygen vacancies. The presence of oxygen vacancies in the pure $NiCo_2O_4$ and Ir_H-$NiCo_2O_4$ samples was further verified by using electron paramagnetic resonance (EPR) spectroscopy (Fig. 2f). The EPR spectra of Ir_H-$NiCo_2O_4$, with a "*g*" value of 2.003, show a symmetric signal strength significantly greater than that of pure $NiCo_2O_4$, suggesting that the synthesized catalyst Ir_H-$NiCo_2O_4$ had a large quantity of oxygen vacancies.

3.2. Acidic OER performance evaluation

The OER performances of pure $NiCo_2O_4$, Ir_L-$NiCo_2O_4$, Ir_H-$NiCo_2O_4$ and commercial IrO_2 were examined using double-layer capacitance (C_{dl}) measurements, electrochemical impedance spectroscopy (EIS), and linear sweep voltammetry (LSV). The optimized electrocatalytic activity of Ir_H-$NiCo_2O_4$ was achieved with $IrCl_3{\cdot}xH_2O$ (4 ml), a reaction temperature of 400 °C, and a reaction time of 2 h (Fig. S6 and S7†). The polarization curves obtained for pure $NiCo_2O_4$, Ir_L-$NiCo_2O_4$, Ir_H-$NiCo_2O_4$ and commercial IrO_2 in 0.5 M H_2SO_4 solution under three-electrode arrangements are shown in Fig. 3a. Ir_H-$NiCo_2O_4$, with an iridium loading of 0.25 mg cm^{-2}, has superior OER performance, exhibiting a low overpotential of 240 mV at a current density of 10 mA cm^{-2}, outperforming pure $NiCo_2O_4$ (370 mV), Ir_L-$NiCo_2O_4$ (255 mV) and commercial IrO_2 (320 mV). The Tafel slope is a critical metric for characterizing the kinetic performance of OER electrocatalysts.[64] Fig. 3b illustrates that Ir_H-$NiCo_2O_4$ exhibits a Tafel slope of 53.05 mV dec^{-1}, much lower than that of pure $NiCo_2O_4$ (117.90 mV dec^{-1}), Ir_L-$NiCo_2O_4$ (71.70 mV dec^{-1}) and commercial IrO_2 (82.59 mV dec^{-1}), suggesting the favorable OER kinetics of Ir_H-$NiCo_2O_4$. At an overpotential of 300 mV, Ir_H-$NiCo_2O_4$ (377.05 mA mg^{-1}) also outperforms Ir_L-$NiCo_2O_4$ (339.40 mA mg^{-1}) and commercial IrO_2 (6.96 mA mg^{-1}) in terms of mass activity (Fig. 3c). This assured an adequate degree of economic viability for Ir_H-$NiCo_2O_4$, which exhibited exceptional electrocatalytic ability while markedly decreasing Ir consumption. Electrochemical impedance spectroscopy and double-layer capacitance (C_{dl}) measurements were employed to evaluate the charge transfer resistance and the electrochemically active

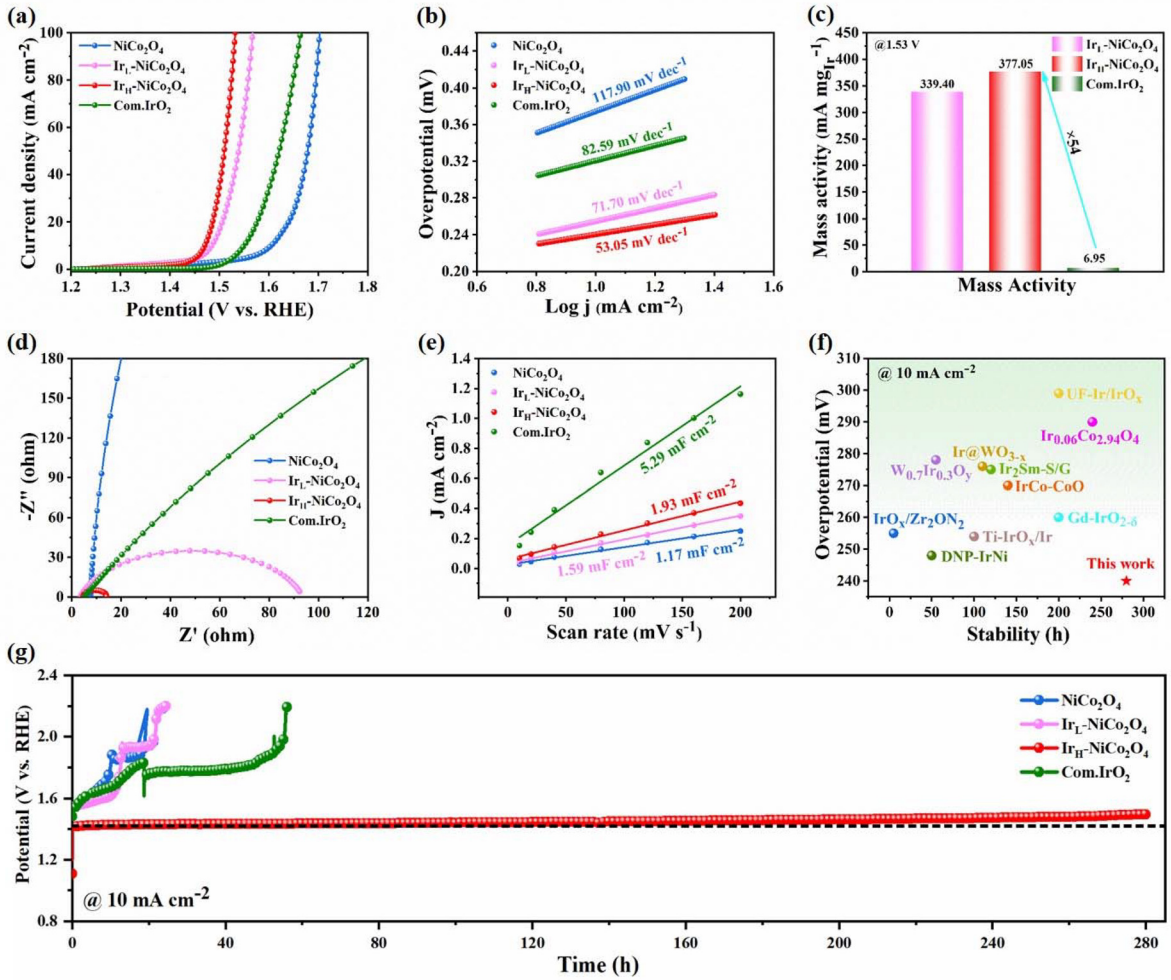

Fig. 3 Electrochemical OER performance in a 0.5 M H_2SO_4 solution. (a) LSV curves of pure $NiCo_2O_4$, Ir_L-$NiCo_2O_4$, Ir_H-$NiCo_2O_4$ and Com.IrO_2. (b) The corresponding Tafel plots. (c) Mass activity at 1.53 V. (d) Nyquist plots. (e) C_{dl} values. (f) Comparison of the overpotential and stability of Ir_H-$NiCo_2O_4$ with previously documented Ir-based electrocatalysts in the literature for the OER in 0.5 M H_2SO_4 at 10 mA cm^{-2}. (g) Chronopotentiometry tests of pure $NiCo_2O_4$, Ir_L-$NiCo_2O_4$, Ir_H-$NiCo_2O_4$ and Com·IrO_2 at 10 mA cm^{-2}.

surface area (ECSA), which further help to identify the cause of enhanced OER activity for Ir_H-$NiCo_2O_4$. Compared to pure $NiCo_2O_4$, Ir_L-$NiCo_2O_4$ and commercial IrO_2, Ir_H-$NiCo_2O_4$ exhibits the smallest semicircle in the low-frequency region, suggesting a faster charge transfer rate of the OER (Fig. 3d).[6]

The electrochemically active surface area (ECSA) was computed from double-layer capacitance (C_{dl}) derived from cyclic voltammetry (CV) curves to provide a more detailed investigation of the electrocatalytic activity of the pure $NiCo_2O_4$, Ir_L-$NiCo_2O_4$, Ir_H-$NiCo_2O_4$ and commercial IrO_2 electrocatalysts. The values of double-layer-capacitance (C_{dl}) for pure $NiCo_2O_4$, Ir_L-$NiCo_2O_4$, Ir_H-$NiCo_2O_4$ and commercial IrO_2 were measured from cyclic voltammetry curves obtained at different scan rates (Fig. S8a–d†). The value of C_{dl} for Ir_H-$NiCo_2O_4$ was 1.93 mF cm^{-2}, which is slightly greater than that of pure $NiCo_2O_4$ (1.17 mF cm^{-2}) and Ir_L-$NiCo_2O_4$ (1.59 mF cm^{-2}) while lower than that of commercial IrO_2 (5.29 mF cm^{-2}) (Fig. 3e). The higher value of C_{dl} revealed that the electrochemically active-surface area (ECSA) of Ir_H-$NiCo_2O_4$ (8.04 cm^{-2}) is larger than that of pure $NiCo_2O_4$ (4.87 cm^{-2}) and Ir_L-$NiCo_2O_4$ (6.62 cm^{-2}). This indicates that Ir_H-$NiCo_2O_4$ has a high ECSA value and tends to expose more effective active sites, which is attributed to its remarkable OER activity. Based on the aforementioned investigation, Ir_H-$NiCo_2O_4$ exhibits enhanced OER performance and improved stability duration for the OER, notably outperforming the most advanced Ir-based electrocatalysts previously documented in the literature (Fig. 3f and Table S3†).[65–74] When assessing its water oxidation performance, long-term stability is a crucial factor to take into account in addition to catalytic activity.[5] Chronopotentiometry has been performed to assess the stability of pure $NiCo_2O_4$, Ir_L-$NiCo_2O_4$, Ir_H-$NiCo_2O_4$ and commercial IrO_2 under acidic conditions applying a constant current density of 10 mA cm^{-2}. Compared to pure $NiCo_2O_4$, Ir_L-$NiCo_2O_4$ and commercial IrO_2, the Ir_H-$NiCo_2O_4$ catalyst exhibited remarkable electrochemical stability even after 282 hours of continuous operation with a minimal degradation rate of only 0.25 mV h^{-1}, demonstrating the good long-term stability of Ir_H-$NiCo_2O_4$ (Fig. 3g). To

further demonstrate the distinct OER mechanism in Ir_H-$NiCo_2O_4$, we performed TMA^+ probe experiments. As shown in Fig. S9,† the addition of TMA^+ had no effect on the OER activity of Ir_H-$NiCo_2O_4$, which indicates that there is no *OO species in the OER process. These results suggest that Ir_H-$NiCo_2O_4$ follows the adsorbate evolution mechanism (AEM).[75]

After the stability test, Ir_H-$NiCo_2O_4$ was characterized by SEM, XRD and XPS to further investigate the morphological and structural changes. The SEM analysis after the stability test for 282 h shows that the morphology of Ir_H-$NiCo_2O_4$ remains unchanged after the stability test, indicating improved stability (Fig. S10†). The XRD pattern also exhibited no significant change after the stability test (Fig. S11†), suggesting that Ir_H-$NiCo_2O_4$ did not fully dissolve in 0.5 M H_2SO_4 solution. Additionally, after the stability test, the XPS spectra of Ir 4f displayed a positive shift in the binding energy, indicating that the surface of Ir had been oxidized (Fig. S12a†). IrO_x on the surface contributes to the OER process by the AEM pathway, and IrO_x also protects the active site from corrosion in the acidic environment. Furthermore, a positive shift of Ni 2p, Co

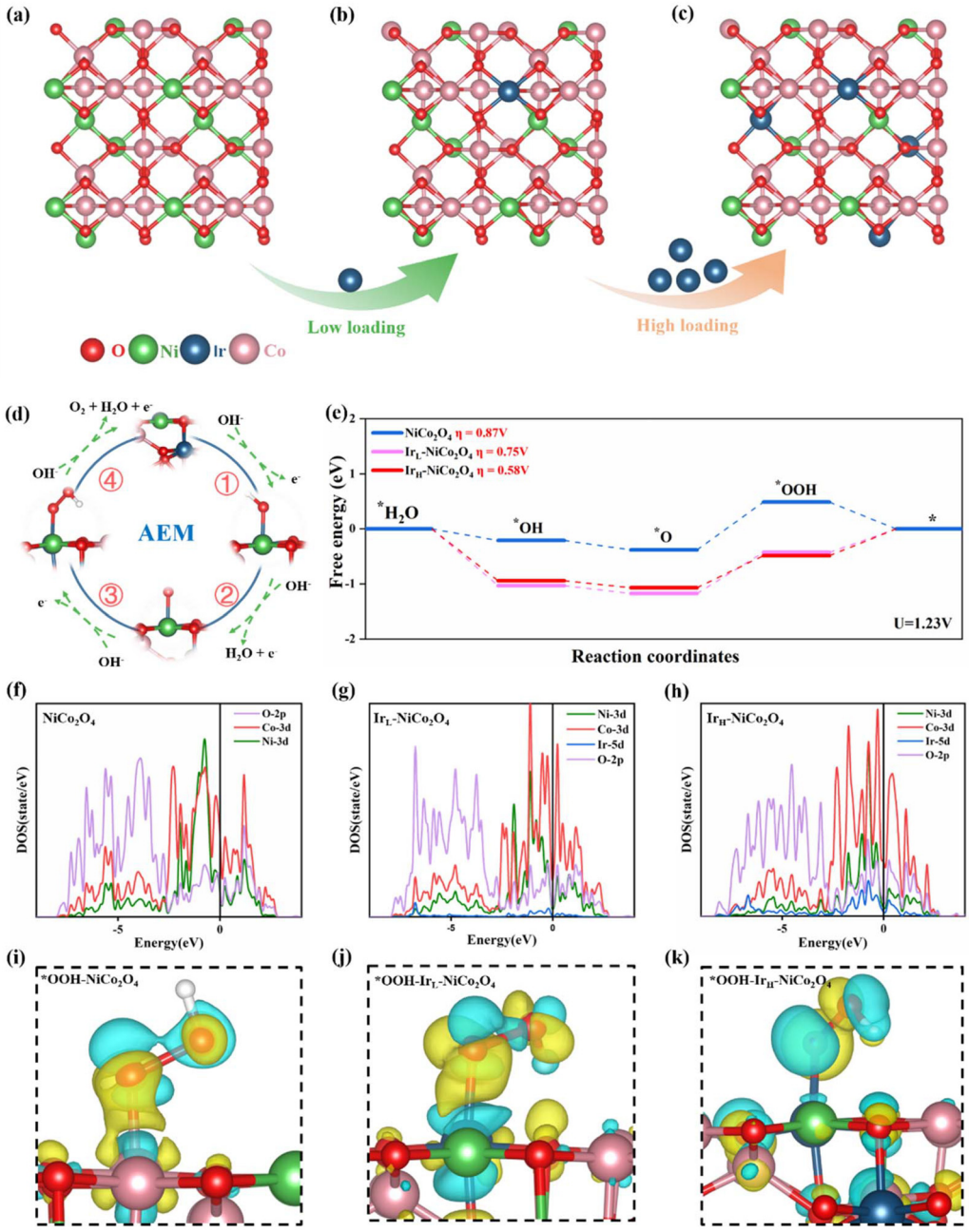

Fig. 4 Density functional theory calculations. (a–c) Atomistic models of $NiCo_2O_4$, Ir_L-$NiCo_2O_4$ and Ir_H-$NiCo_2O_4$. (d) Proposed 4e mechanism of the OER on Ir_H-$NiCo_2O_4$. (e) Free energy diagram of the OER for pure $NiCo_2O_4$, Ir_L-$NiCo_2O_4$ and Ir_H-$NiCo_2O_4$ at U = 1.23 V. (f–h) Calculated DOS of pure $NiCo_2O_4$, Ir_L-$NiCo_2O_4$ and Ir_H-$NiCo_2O_4$. (i–k) Charge density difference analysis for pure $NiCo_2O_4$, Ir_L-$NiCo_2O_4$ and Ir_H-$NiCo_2O_4$.

2p and O 1s in Ir_H-$NiCo_2O_4$ was identified upon this stability test (Fig. S12b–d†).

3.3. Density functional theory calculations

Density functional theory (DFT) simulations were conducted to provide a deeper understanding of the OER performance based on the constructed atomistic structural models of the pristine $NiCo_2O_4$, Ir_L-$NiCo_2O_4$ and Ir_H-$NiCo_2O_4$ catalysts (Fig. 4a–c). To represent the different Ir doping densities, we use $NiCo_2O_4$ with no Ir doping, Ir_L-$NiCo_2O_4$ with a low Ir doping density and Ir_H-$NiCo_2O_4$ with a high Ir doping density, respectively. Fig. 4d illustrates the mechanism and model of the OER carried out by Ir_H-$NiCo_2O_4$, which follows the AEM. Moreover, the catalyst's activity for the OER was assessed by Gibbs free energy analysis at the equilibrium potential (U = 1.23 V). As illustrated in Fig. 4e, the free energy profiles at U = 1.23 V indicated that the energy barrier for the elementary reaction (*O → *OOH) was higher than those of the other three steps (*H_2O → *OH, *OH → *O, and *OOH → *O_2), confirming that *O → *OOH is the rate-determining step (RDS). The calculated overpotential (η) at the rate-determining step (ΔG_{*OOH}) of the Ir_H-$NiCo_2O_4$ catalyst was 0.58 V, which was substantially lower than that of Ir_L-$NiCo_2O_4$ (0.75 V) and pristine $NiCo_2O_4$ (0.87 V). The extremely high density of Ir atoms realized a substantial increase in the OER activity by effectively lowering the free energy barrier of the intermediates, which is consistent with the experimental observations. The partial density of states (PDOS) of Ir_H-$NiCo_2O_4$, Ir_L-$NiCo_2O_4$ and pristine $NiCo_2O_4$ were also computed (Fig. 4f–h). The peak of Co 3d orbitals near the Fermi energy level is driven higher due to the introduction of Ir atoms, which helps electron transport. In addition, as the Ir atomic loading increased, the peak of the Ir 5d orbital can be observed to gradually increase near the Fermi level, which indicates that it also contributes to the enhancement of the electrochemical activity of the catalyst. Meanwhile, the enhanced hybridization of the O 2p orbital with the metal atoms and the corresponding decrease in the antibonding state demonstrate that the introduction of Ir atoms can greatly improve the stability of the catalysts in the acidic OER, which is well matched with the experimental results. Charge density analyses of adsorbed *OOH on the catalysts without Ir doping ($NiCo_2O_4$), with a low Ir doping density (Ir_L-$NiCo_2O_4$) and with a high Ir doping density (Ir_H-$NiCo_2O_4$) are shown in Fig. 4i–k. According to the results, the high-density of Ir single atom doping into the $NiCo_2O_4$ catalyst significantly enhances the OER process by optimizing the adsorption energy of oxygen-containing intermediates.

4. Conclusion

In summary, we have successfully developed a high loading iridium (Ir) single-atom-doped $NiCo_2O_4$ catalyst using an ion-exchange pyrolysis technique. The optimized Ir_H-$NiCo_2O_4$ with a high loading of 7.98 wt% Ir single atoms exhibits exceptional oxygen evolution reaction (OER) performance in acidic media, achieving an overpotential of 240 mV at a current density of 10 mA cm^{-2}. Additionally, it maintains improved catalytic stability for 282 hours, significantly outperforming commercial IrO_2. Furthermore, the Ir_H-$NiCo_2O_4$ catalyst exhibits an Ir-mass activity of 377.05 mA mg_{Ir}^{-1} at an overpotential of 300 mV, surpassing that of commercial IrO_2. Density functional theory calculations show that the high-density of Ir-single atom doping significantly enhances the adsorption energy of oxygen-containing intermediates, thereby promoting the overall OER process. Our study not only highlights the potential of high loading single atom catalysts for the OER in acidic media but also offers new insights into the design and synthesis of advanced SACs.

Conflicts of interest

The authors declare that they have no known competing financial interests or personal relationships that could have appeared to influence the work reported in this paper.

Data availability

Data will be made available on request.

Acknowledgements

The authors gratefully acknowledge the financial support provided by the National Natural Science Foundation of China (No. 12034002, 22279044 and 22202080) and the Jilin Province Science and Technology Development Program (20210301009GX). The authors gratefully acknowledge HZWTECH for providing computational facilities.

References

1 Z. W. Seh, J. Kibsgaard, C. F. Dickens, I. Chorkendorff, J. K. Nørskov and T. F. Jaramillo, Combining theory and experiment in electrocatalysis: Insights into materials design, *Science*, 2017, **355**, eaad4998.
2 S. Chen, T. Takata and K. Domen, Particulate photocatalysts for overall water splitting, *Nat. Rev. Mater.*, 2017, **2**, 1–17.
3 M. Li, X. Zheng, L. Li and Z. Wei, Research progress of hydrogen oxidation and hydrogen evolution reaction mechanism in alkaline media, *Acta Phys.-Chim. Sin.*, 2021, **37**, 2007054.
4 Y. Jin, Z. Zhang, H. Yang, P. Wang, C. Shen, T. Cheng, X. Huang and Q. Shao, Boosting hydrogen production with ultralow working voltage by selenium vacancy–enhanced ultrafine platinum–nickel nanowires, *SmartMat*, 2022, **3**, 130–141.
5 B. Xu, Y. Zhang, Y. Pi, Q. Shao and X. Huang, Research progress of nickel-based metal-organic frameworks and their

derivatives for oxygen evolution catalysis, *Acta Phys.-Chim. Sin.*, 2021, **37**, 2009074.
6 Y. Liu, N. Chen, W. Li, M. Sun, T. Wu, B. Huang, X. Yong, Q. Zhang, L. Gu and H. Song, Engineering the synergistic effect of carbon dots–stabilized atomic and subnanometric ruthenium as highly efficient electrocatalysts for robust hydrogen evolution, *SmartMat*, 2022, **3**, 249–259.
7 J. Chen, Y. Ma, T. Huang, T. Jiang, S. Park, J. Xu, X. Wang, Q. Peng, S. Liu, G. Wang and W. Chen, Ruthenium-Based Binary Alloy with Oxide Nanosheath for Highly Efficient and Stable Oxygen Evolution Reaction in Acidic Media, *Adv. Mater.*, 2024, **36**, 2312369.
8 J. Chen, J. Ma, T. Huang, Q. Liu, X. Liu, R. Luo, J. Xu, X. Wang, T. Jiang, H. Liu, Z. Lv, T. Yao, G. Wang, X. Zheng, Z. Li and W. Chen, Iridium-Free High-Entropy Alloy for Acidic Water Oxidation at High Current Densities, *Angew. Chem., Int. Ed.*, 2025, **64**, e202503330.
9 S. Chu and A. Majumdar, Opportunities and challenges for a sustainable energy future, *Nature*, 2012, **488**, 294–303.
10 M. Carmo, D. L. Fritz, J. Mergel and D. Stolten, A comprehensive review on PEM water electrolysis, *Int. J. Hydrogen Energy*, 2013, **38**, 4901–4934.
11 Y. Jiao, Y. Zheng, M. Jaroniec and S. Z. Qiao, Design of electrocatalysts for oxygen-and hydrogen-involving energy conversion reactions, *Chem. Soc. Rev.*, 2015, **44**, 2060–2086.
12 J. Chen, Y. Ma, C. Cheng, T. Huang, R. Luo, J. Xu, X. Wang, T. Jiang, H. Liu, S. Liu, T. Huang, L. Zhang and W. Chen, Cobalt-Doped Ru@RuO_2 Core–Shell Heterostructure for Efficient Acidic Water Oxidation in Low-Ru-Loading Proton Exchange Membrane Water Electrolyzers, *J. Am. Chem. Soc.*, 2025, **147**, 8720–8731.
13 Z. Li, H. Sheng, Y. Lin, H. Hu, H. Sun, Y. Dong, X. Chen, L. Wei, Z. Tian, Q. Chen, J. Su and L. Chen, Rutile-Structured $Ru_{0.48}Mn_{0.52}O_2$ Solid Solution for Highly Active and Stable Oxygen Evolution at Large Current Density in Acidic Media, *Adv. Funct. Mater.*, 2024, **34**, 2409714.
14 F.-Y. Chen, Z.-Y. Wu, Z. Adler and H. Wang, Stability challenges of electrocatalytic oxygen evolution reaction: From mechanistic understanding to reactor design, *Joule*, 2021, **5**, 1704–1731.
15 S. Hao, H. Sheng, M. Liu, J. Huang, G. Zheng, F. Zhang, X. Liu, Z. Su, J. Hu and Y. Qian, Torsion strained iridium oxide for efficient acidic water oxidation in proton exchange membrane electrolyzers, *Nat. Nanotechnol.*, 2021, **16**, 1371–1377.
16 S. Geiger, O. Kasian, M. Ledendecker, E. Pizzutilo, A. M. Mingers, W. T. Fu, O. Diaz-Morales, Z. Li, T. Oellers and L. Fruchter, The stability number as a metric for electrocatalyst stability benchmarking, *Nat. Catal.*, 2018, **1**, 508–515.
17 B. J. Smith, D. J. Graziano, M. E. Riddle, D.-J. Liu, P. Sun, C. Iloeje, E. Kao and D. Diamond, *Platinum Group Metal Catalysts: Supply Chain Deep Dive Assessment*, USDOE Office of Policy (PO), Washington DC (United States), 2022.
18 L. Zhang, H. Jang, H. Liu, M. G. Kim, D. Yang, S. Liu, X. Liu and J. Cho, Sodium–decorated amorphous/crystalline RuO_2 with rich oxygen vacancies: a robust pH–universal oxygen evolution electrocatalyst, *Angew. Chem.*, 2021, **133**, 18969–18977.
19 H. Hu, S. Liu, H. Sun, W. Sun, J. Tang, L. Wei, X. Chen, Q. Chen, Y. Lin, Z. Tian and J. Su, Low-Ir-Content $Ir_{0.10}Mn_{0.90}O_2$ Solid Solution for Highly Active Oxygen Evolution in Acid Media, *Small*, 2025, **21**, 2412096.
20 A. Wang, J. Li and T. Zhang, Heterogeneous single-atom catalysis, *Nat. Rev. Chem.*, 2018, **2**, 65–81.
21 X.-F. Yang, A. Wang, B. Qiao, J. Li, J. Liu and T. Zhang, Single-atom catalysts: a new frontier in heterogeneous catalysis, *Acc. Chem. Res.*, 2013, **46**, 1740–1748.
22 B. Qiao, A. Wang, X. Yang, L. F. Allard, Z. Jiang, Y. Cui, J. Liu, J. Li and T. Zhang, Single-atom catalysis of CO oxidation using Pt_1/FeO_x, *Nat. Chem.*, 2011, **3**, 634–641.
23 C. Zhu, S. Fu, Q. Shi, D. Du and Y. Lin, Single–atom electrocatalysts, *Angew. Chem., Int. Ed.*, 2017, **56**, 13944–13960.
24 R. Qin, K. Liu, Q. Wu and N. Zheng, Surface coordination chemistry of atomically dispersed metal catalysts, *Chem. Rev.*, 2020, **120**, 11810–11899.
25 J. Xing, J. F. Chen, Y. H. Li, W. T. Yuan, Y. Zhou, L. R. Zheng, H. F. Wang, P. Hu, Y. Wang and H. J. Zhao, Stable isolated metal atoms as active sites for photocatalytic hydrogen evolution, *Chem. – Eur. J.*, 2014, **20**, 2138–2144.
26 H. Wei, X. Liu, A. Wang, L. Zhang, B. Qiao, X. Yang, Y. Huang, S. Miao, J. Liu and T. Zhang, FeO_x-supported platinum single-atom and pseudo-single-atom catalysts for chemoselective hydrogenation of functionalized nitroarenes, *Nat. Commun.*, 2014, **5**, 5634.
27 Y. Li, W. Li, Y. Zhang, H. Huang and Z. Liu, Surficial lattice iridium single atom-strengthened spinel cobalt oxides for acidic water oxidation, *Chem. Eng. J.*, 2025, **503**, 158620.
28 F. Luo, H. Hu, X. Zhao, Z. Yang, Q. Zhang, J. Xu, T. Kaneko, Y. Yoshida, C. Zhu and W. Cai, Robust and stable acidic overall water splitting on Ir single atoms, *Nano Lett.*, 2020, **20**, 2120–2128.
29 J. Wang, Z. Li, Y. Wu and Y. Li, Fabrication of single–atom catalysts with precise structure and high metal loading, *Adv. Mater.*, 2018, **30**, 1801649.
30 D. U. Lee, B. J. Kim and Z. Chen, One-pot synthesis of a mesoporous $NiCo_2O_4$ nanoplatelet and graphene hybrid and its oxygen reduction and evolution activities as an efficient bi-functional electrocatalyst, *J. Mater. Chem. A*, 2013, **1**, 4754–4762.
31 W. Deeloed, T. Priamushko, J. Čížek, S. Suramitr and F. Kleitz, Defect-engineered hydroxylated mesoporous spinel oxides as bifunctional electrocatalysts for oxygen reduction and evolution reactions, *ACS Appl. Mater. Interfaces*, 2022, **14**, 23307–23321.
32 Z. Zhang, X. Liu, D. Wang, H. Wan, Y. Zhang, G. Chen, N. Zhang and R. Ma, Ruthenium composited $NiCo_2O_4$ spinel nanocones with oxygen vacancies as a high-efficient bifunctional catalyst for overall water splitting, *Chem. Eng. J.*, 2022, **446**, 137037.

33 Z. Zhang, X. Liang, J. Li, J. Qian, Y. Liu, S. Yang, Y. Wang, D. Gao and D. Xue, Interfacial engineering of NiO/$NiCo_2O_4$ porous nanofibers as efficient bifunctional catalysts for rechargeable zinc–air batteries, *ACS Appl. Mater. Interfaces*, 2020, **12**, 21661–21669.

34 Y. Wang, L. Chen, H. Zhang, M. Humayun, J. Duan, X. Xu, Y. Fu, M. Bououdina and C. Wang, Elaborately tailored $NiCo_2O_4$ for highly efficient overall water splitting and urea electrolysis, *Green Chem.*, 2023, **25**, 8181–8195.

35 Y. Tao, W. Jiang, H. Wang, W. Hao, Q. Bi, X. Liu, J. Fan and G. Li, Tuning electronic structure of hedgehog-like nickel cobaltite via molybdenum-doping for enhanced electrocatalytic oxygen evolution catalysis, *J. Colloid Interface Sci.*, 2024, **657**, 921–930.

36 H. Hu, B. Y. Guan and X. W. D. Lou, Construction of complex CoS hollow structures with enhanced electrochemical properties for hybrid supercapacitors, *Chem*, 2016, **1**, 102–113.

37 G. Kresse and J. Hafner, Ab initio molecular dynamics for liquid metals, *Phys. Rev. B*, 1993, **47**, 558.

38 G. Kresse and J. Furthmüller, Efficient iterative schemes for ab initio total-energy calculations using a plane-wave basis set, *Phys. Rev. B*, 1996, **54**, 11169.

39 P. E. Blochl, Projector augmented-wave method, *Phys. Rev. B*, 1994, **50**, 17953–17979.

40 G. Kresse and D. Joubert, From ultrasoft pseudopotentials to the projector augmented-wave method, *Phys. Rev. B*, 1999, **59**, 1758.

41 J. P. Perdew, K. Burke and M. Ernzerhof, Generalized gradient approximation made simple, *Phys. Rev. Lett.*, 1996, **77**, 3865.

42 S. Grimme, Semiempirical GGA–type density functional constructed with a long–range dispersion correction, *J. Comput. Chem.*, 2006, **27**, 1787–1799.

43 J. K. Nørskov, J. Rossmeisl, A. Logadottir, L. Lindqvist, J. R. Kitchin, T. Bligaard and H. Jonsson, Origin of the overpotential for oxygen reduction at a fuel-cell cathode, *J. Phys. Chem. B*, 2004, **108**, 17886–17892.

44 A. A. Peterson, F. Abild-Pedersen, F. Studt, J. Rossmeisl and J. K. Nørskov, How copper catalyzes the electroreduction of carbon dioxide into hydrocarbon fuels, *Energy Environ. Sci.*, 2010, **3**, 1311–1315.

45 M. Iliev, P. Silwal, B. Loukya, R. Datta, D. Kim, N. Todorov, N. Pachauri and A. Gupta, Raman studies of cation distribution and thermal stability of epitaxial spinel $NiCo_2O_4$ films, *J. Appl. Phys.*, 2013, **114**, 033514.

46 S. V. Tatarin, P. Kalle, I. V. Taydakov, E. A. Varaksina, V. M. Korshunov and S. I. Bezzubov, Sterically hindered phenanthroimidazole ligands drive the structural flexibility and facile ligand exchange in cyclometalated iridium(III) complexes, *Dalton Trans.*, 2021, **50**, 6889–6900.

47 J. Clancy, N. Chen, C. Kim, W. Chen, K. Plumb, B. Jeon, T. Noh and Y.-J. Kim, Spin-orbit coupling in iridium-based 5 d compounds probed by X-ray absorption spectroscopy, *Phys. Rev. B*, 2012, **86**, 195131.

48 K. Kojima, R. Kadono, M. Miyazaki, M. Hiraishi, I. Yamauchi, A. Koda, Y. Tsuchiya, H. Suzuki and H. Kitazawa, Magnetic frustration in iridium spinel compound $CuIr_2S_4$, *Phys. Rev. Lett.*, 2014, **112**, 087203.

49 H. Kuriyama, J. Matsuno, S. Niitaka, M. Uchida, D. Hashizume, A. Nakao, K. Sugimoto, H. Ohsumi, M. Takata and H. Takagi, Epitaxially stabilized iridium spinel oxide without cations in the tetrahedral site, *Appl. Phys. Lett.*, 2010, **96**, 182103.

50 Y. Zhao, M. Luo, S. Chu, M. Peng, B. Liu, Q. Wu, P. Liu, F. M. de Groot and Y. Tan, 3D nanoporous iridium-based alloy microwires for efficient oxygen evolution in acidic media, *Nano Energy*, 2019, **59**, 146–153.

51 Y. Yuan, J. Wang, S. Adimi, H. Shen, T. Thomas, R. Ma, J. P. Attfield and M. Yang, Zirconium nitride catalysts surpass platinum for oxygen reduction, *Nat. Mater.*, 2020, **19**, 282–286.

52 J. Shan, C. Guo, Y. Zhu, S. Chen, L. Song, M. Jaroniec, Y. Zheng and S.-Z. Qiao, Charge-redistribution-enhanced nanocrystalline Ru@IrO_x electrocatalysts for oxygen evolution in acidic media, *Chem*, 2019, **5**, 445–459.

53 H.-S. Oh, H. N. Nong, T. Reier, A. Bergmann, M. Gliech, J. Ferreira de Araújo, E. Willinger, R. Schlögl, D. Teschner and P. Strasser, Electrochemical catalyst–support effects and their stabilizing role for IrO_x nanoparticle catalysts during the oxygen evolution reaction, *J. Am. Chem. Soc.*, 2016, **138**, 12552–12563.

54 R. Li, H. Wang, F. Hu, K. Chan, X. Liu, Z. Lu, J. Wang, Z. Li, L. Zeng and Y. Li, IrW nanochannel support enabling ultrastable electrocatalytic oxygen evolution at 2 A cm^{-2} in acidic media, *Nat. Commun.*, 2021, **12**, 3540.

55 Y. Qin, T. Yu, S. Deng, X.-Y. Zhou, D. Lin, Q. Zhang, Z. Jin, D. Zhang, Y.-B. He and H.-J. Qiu, RuO_2 electronic structure and lattice strain dual engineering for enhanced acidic oxygen evolution reaction performance, *Nat. Commun.*, 2022, **13**, 3784.

56 R. Chen, H.-Y. Wang, J. Miao, H. Yang and B. Liu, A flexible high-performance oxygen evolution electrode with three-dimensional $NiCo_2O_4$ core-shell nanowires, *Nano Energy*, 2015, **11**, 333–340.

57 J. Marco, J. Gancedo, M. Gracia, J. Gautier, E. Ríos and F. Berry, Characterization of the nickel cobaltite, $NiCo_2O_4$, prepared by several methods: an XRD, XANES, EXAFS, and XPS study, *J. Solid State Chem.*, 2000, **153**, 74–81.

58 K. Du, L. Zhang, J. Shan, J. Guo, J. Mao, C.-C. Yang, C.-H. Wang, Z. Hu and T. Ling, Interface engineering breaks both stability and activity limits of RuO2 for sustainable water oxidation, *Nat. Commun.*, 2022, **13**, 5448.

59 Y. Yu, H. Li, J. Liu, W. Xu, D. Zhang, J. Xiong, B. Li, A. Omelchuk, J. Lai and L. Wang, High entropy stabilizing lattice oxygen participation of Ru-based oxides in acidic water oxidation, *J. Mater. Chem. A*, 2022, **10**, 21260–21265.

60 Z. Xiao, Y.-C. Huang, C.-L. Dong, C. Xie, Z. Liu, S. Du, W. Chen, D. Yan, L. Tao, Z. Shu, G. Zhang, H. Duan, Y. Wang, Y. Zou, R. Chen and S. Wang, Operando Identification of the Dynamic Behavior of Oxygen Vacancy-

Rich Co_3O_4 for Oxygen Evolution Reaction, *J. Am. Chem. Soc.*, 2020, **142**, 12087–12095.

61 D. A. Kuznetsov, M. A. Naeem, P. V. Kumar, P. M. Abdala, A. Fedorov and C. R. Müller, Tailoring Lattice Oxygen Binding in Ruthenium Pyrochlores to Enhance Oxygen Evolution Activity, *J. Am. Chem. Soc.*, 2020, **142**, 7883–7888.

62 Z. Wang, W. Wang, L. Zhang and D. Jiang, Surface oxygen vacancies on Co3O4 mediated catalytic formaldehyde oxidation at room temperature, *Catal. Sci. Technol.*, 2016, **6**, 3845–3853.

63 E. Ramos-Moore, P. Ferrari, D. E. Diaz-Droguett, D. Lederman and J. T. Evans, Raman and X-ray photoelectron spectroscopy study of ferroelectric switching in Pb(Nb,Zr,Ti)O_3 thin films, *J. Appl. Phys.*, 2012, **111**, 014108.

64 F. Yang, T. Xiong, P. Huang, S. Zhou, Q. Tan, H. Yang, Y. Huang and M.-S. J. T. Balogun, Nanostructured transition metal compounds coated 3D porous core-shell carbon fiber as monolith water splitting electrocatalysts: a general strategy, *Chem. Eng. J.*, 2021, **423**, 130279.

65 K.-R. Yeo, K.-S. Lee, H. Kim, J. Lee and S.-K. Kim, A highly active and stable 3D dandelion spore-structured self-supporting Ir-based electrocatalyst for proton exchange membrane water electrolysis fabricated using structural reconstruction, *Energy Environ. Sci.*, 2022, **15**, 3449–3461.

66 J. Shan, C. Ye, S. Chen, T. Sun, Y. Jiao, L. Liu, C. Zhu, L. Song, Y. Han and M. Jaroniec, Short-range ordered iridium single atoms integrated into cobalt oxide spinel structure for highly efficient electrocatalytic water oxidation, *J. Am. Chem. Soc.*, 2021, **143**, 5201–5211.

67 C. Lee, K. Shin, Y. Park, Y. H. Yun, G. Doo, G. H. Jung, M. Kim, W. C. Cho, C. H. Kim and H. M. Lee, Catalyst–Support Interactions in Zr_2ON_2–Supported IrO_x Electrocatalysts to Break the Trade–Off Relationship Between the Activity and Stability in the Acidic Oxygen Evolution Reaction, *Adv. Funct. Mater.*, 2023, **33**, 2301557.

68 J. Wu, W. Zou, J. Zhang, L. Zhang, H. Song, Z. Cui and L. Du, Regulating Ir–O Covalency to Boost Acidic Oxygen Evolution Reaction, *Small*, 2024, **20**, 2308419.

69 T. Yan, S. Chen, W. Sun, Y. Liu, L. Pan, C. Shi, X. Zhang, Z.-F. Huang and J.-J. Zou, IrO_2 nanoparticle-decorated Ir-doped W18O49 nanowires with high mass specific OER activity for proton exchange membrane electrolysis, *ACS Appl. Mater. Interfaces*, 2023, **15**, 6912–6922.

70 B. Zaman, J. Fan, D. Wang, H. Fan, M. Gong, M. Faizan and X. Cui, Surface–Segregated IrCo Nanoparticles on CoO Nanosheets with Ultralow Ir Loading for Efficient Acidic Water Splitting, *ChemCatChem*, 2024, **16**, e202400795.

71 A. Chen, M. Deng, Z. Lu, Y. Lin and L. Chen, Ultrafine iridium nanoparticles prepared without a surfactant for the acidic oxygen evolution reaction, *Mater. Chem. Front.*, 2023, **7**, 4900–4907.

72 X. Ma, C. Yang, F. Zhang, F. Ke, Q. Cheng, L. Zou and H. Yang, Oxygen-vacancy-rich tungsten oxide boosted ultrasmall iridium nanoparticles for acidic oxygen evolution, *Int. J. Hydrogen Energy*, 2023, **48**, 36776–36783.

73 S. Zhang, L. Yin, Q. Li, S. Wang, W. Wang and Y. Du, Laves phase Ir_2 Sm intermetallic nanoparticles as a highly active electrocatalyst for acidic oxygen evolution reaction, *Chem. Sci.*, 2023, **14**, 5887–5893.

74 X. Wang, Z. Qin, J. Qian, L. Chen and K. Shen, IrCo nanoparticles encapsulated with carbon nanotubes for efficient and stable acidic water splitting, *ACS Catal.*, 2023, **13**, 10672–10682.

75 T. Gao, D. Jiao, L. Wang, X. Ge, X. Wen, L. Zhang, L. Zheng, X. Zou, W. Zhang, W. Zheng, J. Fan and X. Cui, Switchable Acidic Oxygen Evolution Mechanisms on Atomic Skin of Ruthenium Metallene Oxides, *J. Am. Chem. Soc.*, 2025, **147**, 4159–4166.